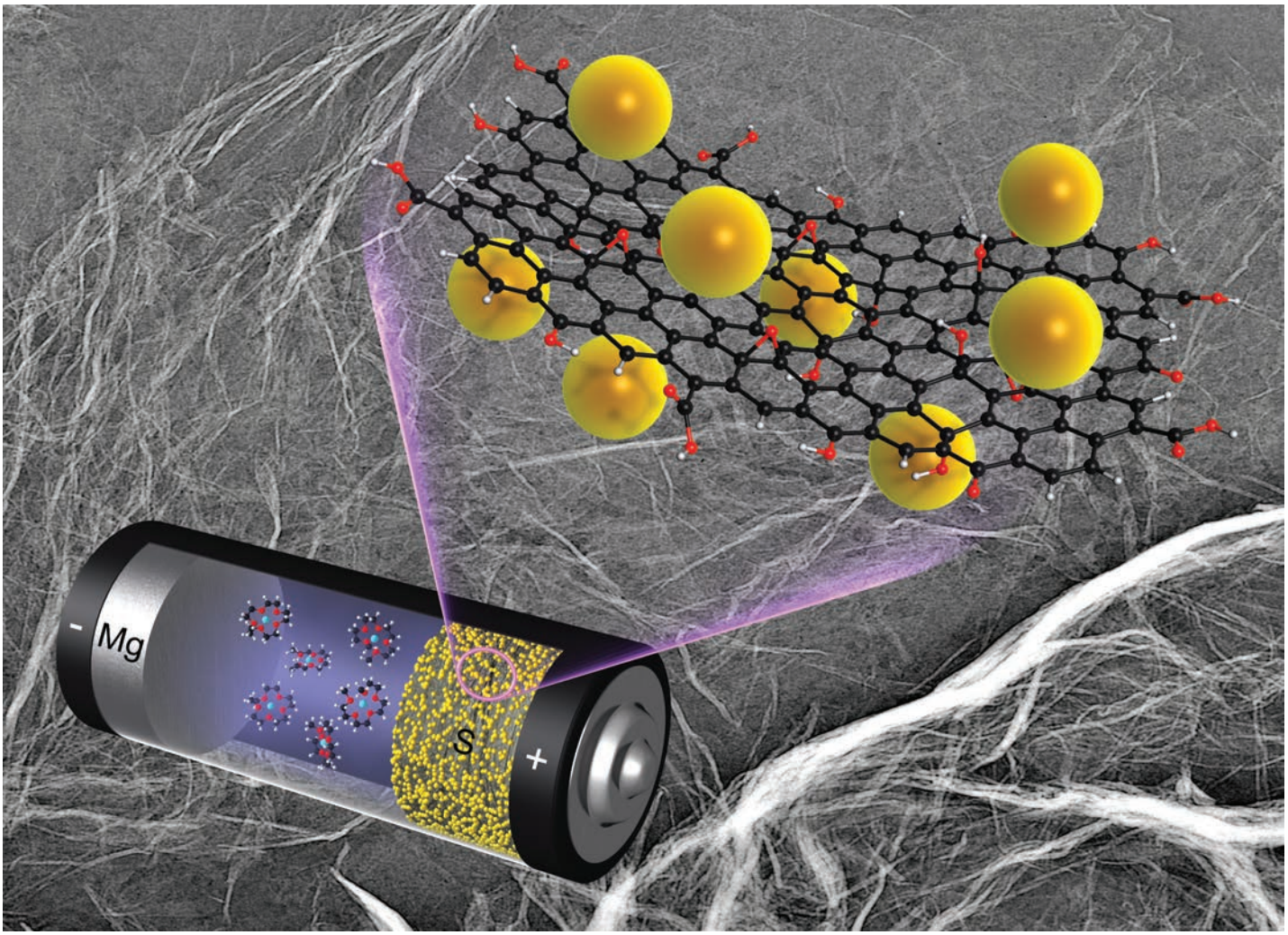


**Showcasing research from the Helmholtz Institute Ulm for Electrochemical Energy Storage (HIU).**

Title: Performance study of magnesium–sulfur battery using a graphene based sulfur composite cathode electrode and a non-nucleophilic Mg electrolyte

Rechargeable magnesium–sulfur (Mg/S) batteries are promising for electric vehicle applications and better electrochemical energy storage of renewable energies due to the inherent merits associated with these battery electrode materials, such as natural abundance, operational safety and high theoretical capacity (1671 mAh $g^{-1}$ or 3459 mAh $cm^{-3}$). Here we show the electrochemical performance and working mechanism of an Mg/S rechargeable battery using a sulfur dispersed graphene nanocomposite as the cathode and a non-nucleophilic Mg based complex in a tetraglyme solvent as the electrolyte.

## As featured in:

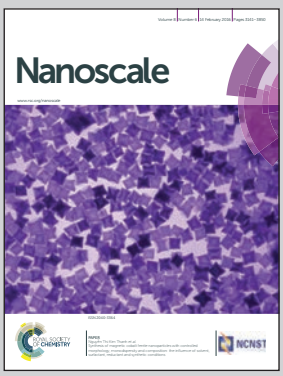


See B. P. Vinayan, Maximilian Fichtner *et al*. *Nanoscale*, 2016, **8**, 3295.

ROYAL SOCIETY OF CHEMISTRY

www.rsc.org/nanoscale

Registered charity number: 207890

Nanoscale

PAPER

View Article Online
View Journal | View Issue

Open Access Article. Published on 28 October 2015. Downloaded on 6/14/2026 5:48:44 AM.
This article is licensed under a Creative Commons Attribution 3.0 Unported Licence.

Cite this: *Nanoscale*, 2016, **8**, 3296

# Performance study of magnesium–sulfur battery using a graphene based sulfur composite cathode electrode and a non-nucleophilic Mg electrolyte†

B. P. Vinayan,*[a] Zhirong Zhao-Karger,[b] Thomas Diemant,[c] Venkata Sai Kiran Chakravadhanula,[a,b,d] Nele I. Schwarzburger,[a] Musa Ali Cambaz,[a] R. Jürgen Behm,[a,c] Christian Kübel[a,b,d] and Maximilian Fichtner*[a,b]

Received 1st July 2015,
Accepted 25th October 2015

DOI: 10.1039/c5nr04383b

www.rsc.org/nanoscale

Here we report for the first time the development of a Mg rechargeable battery using a graphene–sulfur nanocomposite as the cathode, a Mg–carbon composite as the anode and a non-nucleophilic Mg based complex in tetraglyme solvent as the electrolyte. The graphene–sulfur nanocomposites are prepared through a new pathway by the combination of thermal and chemical precipitation methods. The Mg/S cell delivers a higher reversible capacity (448 mA h $g^{-1}$), a longer cyclability (236 mA h $g^{-1}$ at the end of the 50$^{th}$ cycle) and a better rate capability than previously described cells. The dissolution of Mg polysulfides to the anode side was studied by X-ray photoelectron spectroscopy. The use of a graphene–sulfur composite cathode electrode, with the properties of a high surface area, a porous morphology, a very good electronic conductivity and the presence of oxygen functional groups, along with a non-nucleophilic Mg electrolyte gives an improved battery performance.

## 1. Introduction

Rechargeable magnesium (Mg) batteries have been proposed for use in the electrochemical energy storage of renewable energy and realization of electric vehicles owing to the inherent merits associated with Mg such as natural abundance, operational safety and a high volumetric capacity. Among different kinds of alkaline/alkaline earth metal anodes, magnesium (Mg) has the highest theoretical volumetric capacity (3832 mA h $cm^{-3}$) and a high negative reduction potential of −2.356 V *versus* a normal hydrogen electrode (NHE). For comparison, the graphite anodes presently used in lithium ion batteries (LIBs) have a volumetric capacity of only 777 mA h $cm^{-3}$.[1] Mg as an anode material can be considered a safer electrode in liquid electrolytes because it does not form dendrites as compared to lithium.[2] Theoretical calculations show that Mg favors the growth of smooth surfaces as compared to Li and Na due to its lower diffusion barriers and higher-coordinated configurations.[3] In addition, the raw material for Mg is cheaper than for lithium and its compounds are usually non-toxic.

Among the different types of cathode materials, sulfur (S) would be a promising cathode for Mg based rechargeable batteries owing to its high theoretical capacity (1671 mA h $g^{-1}$ or 3459 mA h $cm^{-3}$) and natural abundance. The combination of a Mg anode and a sulfur cathode yields a theoretical volumetric energy density of 3200 Wh $l^{-1}$ as compared to 2800 Wh $l^{-1}$ for a lithium–sulfur battery.[1,4] However, a number of issues have to be addressed for the realization of a Mg/S rechargeable battery system. A challenge, which has limited the development of rechargeable Mg/S batteries, was the availability of suitable electrolytes with a high ionic conductivity, wherein Mg could be deposited reversibly.[5] This is mainly due to the strong electrophilic nature of sulfur, which demands a non-nucleophilic electrolyte. Muldoon *et al.* succeeded in developing a non-nucleophilic electrolyte by the addition of $AlCl_3$ to the THF solution of hexamethyldisilazide magnesium chloride and tested the first Mg/S battery cell for two cycles with

[a]*Helmholtz Institute Ulm for Electrochemical Energy Storage (HIU), Helmholtzstr. 11, D-89081 Ulm, Germany. E-mail: vinayan.parambath@kit.edu, maximilian.fichtner@kit.edu; Fax: +49 (0)731 50 34299; Tel: +49 (0)731 50 34201*
[b]*Institute of Nanotechnology, Karlsruhe Institute of Technology (KIT), P.O. Box 3640, D-76021 Karlsruhe, Germany*
[c]*Institute of Surface Chemistry and Catalysis, Ulm University, Albert-Einstein-Allee 47, D-89081 Ulm, Germany*
[d]*Karlsruhe Nano Micro Facility, Karlsruhe Institute of Technology, D-76344 Eggenstein-Leopoldshafen, Germany*
†Electronic supplementary information (ESI) available. See DOI: 10.1039/c5nr04383b


This journal is © The Royal Society of Chemistry 2016

Open Access Article. Published on 28 October 2015. Downloaded on 6/14/2026 5:48:44 AM.
This article is licensed under a Creative Commons Attribution 3.0 Unported Licence.

discharge capacities of 1200 mA h $g^{-1}$ and 394 mA h $g^{-1}$, respectively, at a discharge voltage of around 1 V.[1] Recently, Zhao-Karger *et al.* reported a non-nucleophilic electrolyte for a Mg/S battery based on a non-nucleophilic base of magnesium-bis(hexamethyldisilazide) [$(HMDS)_2Mg$] transmetallated with $AlCl_3$ as a Lewis acid (1 : 2 molar ratio) and dissolved the reaction product in different ethereal solvents.[6] Using these electrolytes, the discharge potential of the Mg/S battery was improved up to 1.65 V, which is close to the thermodynamic value of voltage (~1.7 V).[7]

The first studies on a Mg/S rechargeable battery indicated issues like polarization effects during charging, low cyclic stability, initial capacity fading and polysulfide dissolution, analogous to the Li/S battery system.[8,9] In Li/S batteries, the soluble polysulfides led to self-discharge and degradation of the cell.[10,11] The electrical insulating property of the sulfur material is another problem that gives a low electronic charge transfer to the current collectors. To address some of these issues it is necessary to design a composite of nanodispersed active sulfur material in a suitable carbon host matrix. The carbon host material needs to have (a) a strong chemical anchoring of sulfur and subsequently formed polysulfides, (b) a high electrical conductivity, (c) a mechanically stable framework to uphold the strain generated by the volume changes of sulfur during the cycling, (d) easy access of the liquid electrolyte to the sulfur active material, and (e) small pores without big openings to accommodate polysulfides. Among different types of carbon nanomaterials, graphene (G) based nanostructures have emerged as preferred materials for energy storage applications due to their unique properties such as a large surface area, a high charge mobility, excellent electronic and thermal conductivity, a high mechanical strength and good chemical stability.[12–14]

In this paper, we have investigated the cell performance and working mechanism of a reduced graphene oxide/sulfur nanocomposite cathode material in a Mg/S rechargeable battery system using a non-nucleophilic Mg electrolyte. The rGO–sulfur nanocomposite has been prepared by a combination of thermal and chemical precipitation methods.

## 2. Experimental

### 2.1 Material synthesis

**2.1(a) Preparation of a sulfur-reduced graphene oxide nanocomposite (S-rGO).** Reduced graphene oxide (rGO) was prepared by thermal exfoliation of graphite oxide (GO) at 400 °C under an argon gas atmosphere, where GO was initially synthesized by Hummer's method.[15] Sodium polysulfide ($Na_2S_x$) solution was prepared by dissolving 1.29 g of sodium sulfide powder ($Na_2S$, anhydrous, Alfa Aesar) in 50 ml of Millipore water and subsequently adding 1.6 g of sublimed sulfur (99.5%, Alfa Aesar) to this solution and dispersing it well by ultra-sonication and stirring. The change in the color of the solution from yellow to orange during the dissolution of sulfur indicates the formation of sodium polysulfide solution. Next, 0.2 g of rGO was dispersed in 200 ml of deionized water by ultra-sonication and a $Na_2S_x$ solution was added dropwise to the rGO solution using a burette while stirring. The rGO–$Na_2S_x$ solution was continuously stirred for the next 24 h. Then, 200 ml of 2 M formic acid (HCOOH, ≥96%, Sigma-Aldrich) was slowly added to the rGO–$Na_2S_x$ solution using a burette while stirring and was allowed to stir for an additional 6 h. The final sample was filtered, washed and dried at 50 °C in a vacuum for 12 h. Then this sample was heat-treated initially at 160 °C for 4 h and further heated at 300 °C for 1 h under an argon atmosphere.

**2.1(b) Preparation of the magnesium–carbon composite (Mg–C).** Magnesium powder (magnesium powder, 325 mesh, 99.8%, Alfa Aesar) and conductive carbon black (TIMCAL C-NERGY SUPER C65) were ball milled together in the weight ratio 80 : 20 using a planetary ball-mill (Fritsch PULVERISETTE 6) with an 80 ml silicon nitride vial and silicon nitride balls under an argon atmosphere at 200 rpm for 12 h.

**2.1(c) Synthesis of the electrolyte.** The synthesis procedure was carried out in an argon filled glove box and is explained in detail in our previous paper.[6] In brief, magnesium-bis(hexamethyldisilazide) [97%, Sigma-Aldrich] (1.24 g) was dissolved in 4 mL of tetraglyme [anhydrous, ≥99%, Aldrich] in a glass vial. Subsequently anhydrous $AlCl_3$ [99.999%, Sigma-Aldrich] (0.96 g) was slowly added to this solution and stirred for the next 36 h at room temperature. After that, $MgCl_2$ [anhydrous, Sigma-Aldrich] (0.343 g) was added to the solution and continuously stirred for 48 h.

### 2.2 Characterization of materials

The X-ray diffraction (XRD) measurements were conducted on a Stadi P diffractometer (STOE & Cie) with a Mythen detector using a Cu $K_\alpha$ X-ray source. Raman measurements were carried out with a confocal Raman microscope (InVia, Renishaw) in the spectral range 800–2000 $cm^{-1}$ using a 532 nm laser excitation source. Thermogravimetric analysis (TGA) of the samples was carried out along with differential scanning calorimetry (DSC) using a Setaram thermal analyzer SENSYS evo instrument. The measurements were conducted from room temperature to 600 °C under helium flow (20 ml $min^{-1}$) at a heating rate of 10 °C $min^{-1}$. To identify different functional groups within the samples, FTIR experiments were performed using a FTIR spectrometer (Spectrum Two, PerkinElmer) in the spectral range of 500–4000 $cm^{-1}$.

The morphological studies of the samples were conducted using a scanning electron microscope (SEM, LEO Gemini 1550 VP) and a transmission electron microscope (TEM). TEM characterization of the nanocomposite was carried out using an aberration corrected FEI Titan 80-300 operated at 80 kV and 300 kV and equipped with a Gatan imaging filter (Tridiem 863). For (S)-TEM measurements, samples were prepared by dispersing a small amount of powder directly onto holey carbon Au grids (Quantifoil).

The chemical state of the sample surfaces was determined by X-ray Photoelectron Spectroscopy (XPS) measurements using monochromatized Al $K_\alpha$ (1486.6 eV) radiation (PHI 5800

Open Access Article. Published on 28 October 2015. Downloaded on 6/14/2026 5:48:44 AM.
This article is licensed under a Creative Commons Attribution 3.0 Unported Licence.

MultiTechnique ESCA System, Physical Electronics). The measurements were performed with a detection angle of 45°, using pass energies at the analyzer of 93.9 and 29.35 eV for survey and detail spectra, respectively. The samples were neutralized with electrons from a flood gun (current 3 μA) to compensate for charging effects at the surface. For binding energy calibration the C(1s) peak of the graphene was set at 284.5 eV. To avoid surface contamination, the samples were transferred under an inert gas atmosphere to the sample load lock of the XPS system.

### 2.3 Electrochemical measurements

The cathode electrodes were prepared by mixing 75 wt% of S–rGO with 10 wt% polyvinylidenefluoride (PVDF, Kynar) binder and 15 wt% Super P carbon, using *N*-methyl-2-pyrrolidinone (NMP, Sigma-Aldrich) as the solvent. The slurry was uniformly coated over an Inconel 625 current collector disk (10 mm diameter) and dried at 60 °C for 24 h to remove the solvent. Electrochemical measurements were conducted using a Swagelok type cell with S–rGO as a cathode electrode, Mg–carbon composite pellets (10 mm) as an anode electrode, Celgard 2500 as the separator, and a non-nucleophilic electrolyte. The whole assembly of the cells was conducted in an argon filled glove box (MBRAUN) with a recirculation unit. Galvanostatic charge–discharge measurements were performed using an electrochemical workstation (Arbin Instruments) between 2.5 and 0.5 V *vs.* $Mg^{2+}$/Mg at room temperature.

## 3. Results and discussion

Fig. 1 shows a schematic diagram of the impregnation of sulfur atoms to the reduced graphene oxide (rGO) structures, where rGO was prepared by thermal exfoliation of graphite oxide (GO) at 400 °C under an argon atmosphere. Since exfoliation of GO is done at moderate temperatures, the process retains some amount of various oxygen functional groups such as hydroxyl, epoxide, carbonyl, and carboxyl groups over the surface of the graphene layers. The presence of various oxygen functional groups over rGO was later confirmed by FTIR and XPS characterization techniques (see the discussion below). Sulfur was dispersed over rGO by a chemical precipitation method using sodium polysulfide ($Na_2S_x$) as the sulfur source and formic acid (HCOOH) as the reducing agent in aqueous media. Initial heat treatment of this composite at 160 °C for 4 h causes the melting of sulfur and its subsequent diffusion over the layers and into the pores of rGO. Further heat treatment of this composite at 300 °C for 1 h helps to remove the non-adsorbed sulfur particles from the graphene surface and also to control the sulfur loading within the composite. During this process, the sulfur is dispersed uniformly over graphene layers because of (a) its 2 dimensional high surface area morphology, (b) its porous structure, and (c) the presence of various oxygen functional groups over rGO.

The XRD patterns of rGO, sublimed sulfur and S–rGO nanocomposite are shown in Fig. 2. The broad peak of rGO, ranging from 14° to 30°, is an indication of the loss of crystallinity through the (002) graphitic plane and the formation of stacked layers of graphene. After thermal exfoliation, the (002) *d* spacing of rGO was increased to 3.55 Å as compared to the starting graphite (*d* = 3.35 Å).[16] XRD of sublimed sulfur gives the main peaks centered at $2\theta$ = 23.4° and 28.0°, and matches well with the (222) and (040) reflections of the *Fddd* orthorhombic phase (JCPSD no. 08-0247). The sharp and strong diffraction peaks of sublimed sulfur confirm the well-defined crystal structure. The XRD pattern of the S–rGO nanocomposite did not exhibit any sulfur peaks, which is probably due to the confinement of sulfur within the pores of rGO.

Raman spectroscopy is a powerful analytical tool for carbon materials to evaluate the degree of graphitic order and doping.[17] rGO and S–rGO samples showed two main peaks

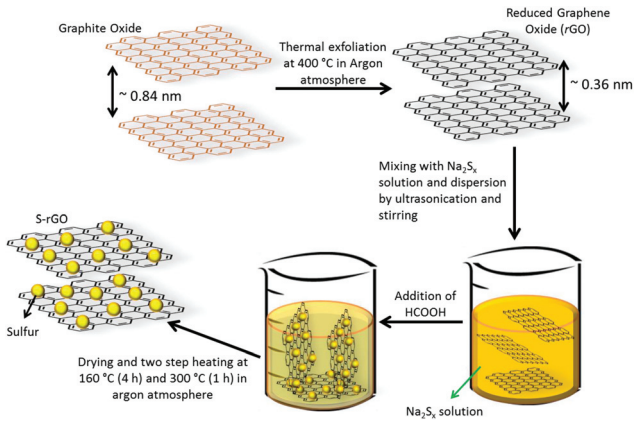


Fig. 1 Schematic diagram of the procedure adopted for synthesizing graphene based sulfur nanocomposite.

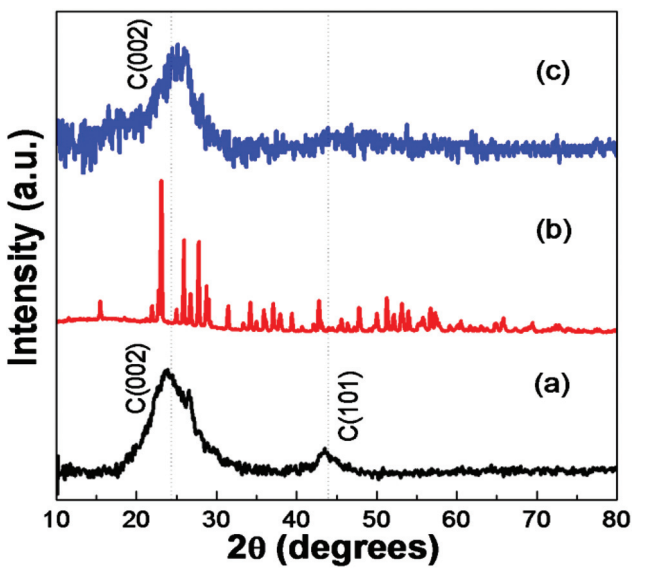


Fig. 2 X-ray diffractograms of (a) rGO, (b) sulfur, and (c) S–rGO nanocomposite.


This journal is © The Royal Society of Chemistry 2016

Open Access Article. Published on 28 October 2015. Downloaded on 6/14/2026 5:48:44 AM.
This article is licensed under a Creative Commons Attribution 3.0 Unported Licence.

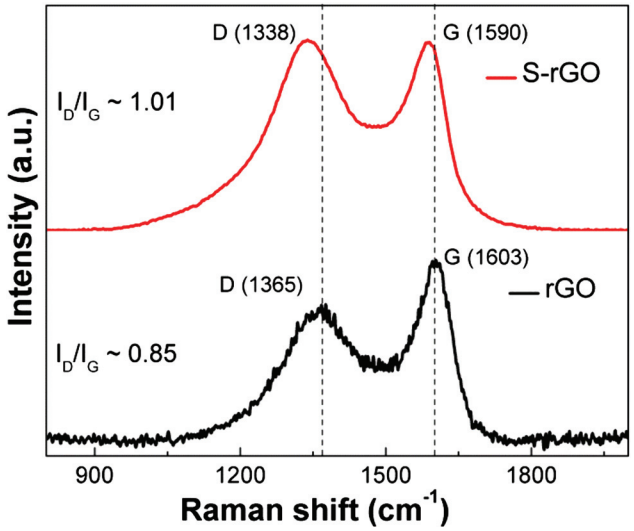


Fig. 3 Raman spectra of rGO and S–rGO nanocomposite.

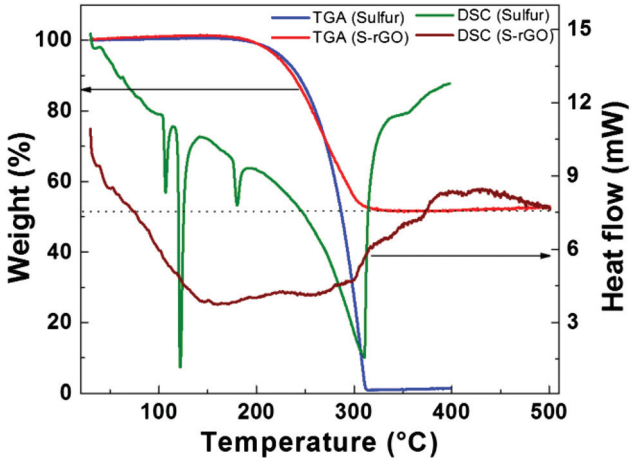


Fig. 4 TGA-DSC analysis of sulfur and S–rGO nanocomposites under 20 ml min$^{-1}$ helium flow and 10 °C min$^{-1}$ heating rate.

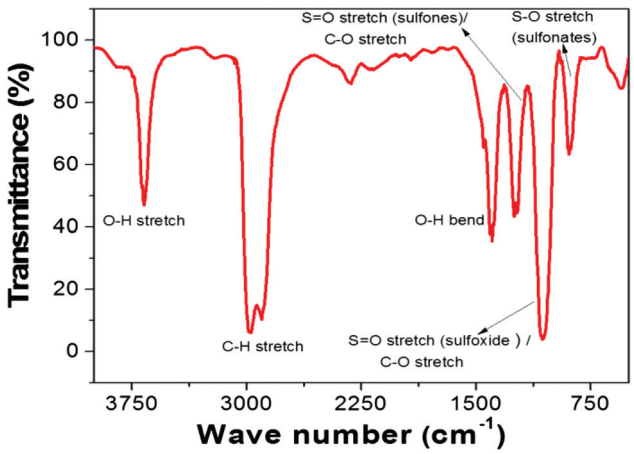


Fig. 5 FTIR spectrum of the S–rGO nanocomposite.

corresponding to the G and D bands as shown in Fig. 3. The G band is due to the Raman active $E_{2g}$ mode and measures the crystallinity of a carbon material. The D band represents the breathing mode of the $sp^2$ ring of the graphene layers, which is sensitive to different kinds of structural and heteroatom doping defects.[17] The intensity ratio between D and G bands ($I_D/I_G$) is usually used to measure the defect density in the carbon nanostructures. The $I_D/I_G$ ratios for rGO and S–rGO samples were 0.85 and 1.01, respectively, and the increased $I_D/I_G$ ratio for the S–rGO sample is ascribed to an enhanced structural distortion caused by S doping within the graphene lattice. The peak positions for the G band in rGO and S–rGO samples were at 1603 cm$^{-1}$ and 1590 cm$^{-1}$, *i.e.*, a downward shift of 13 cm$^{-1}$ was observed after S doping. A similar downward shift of the G band has been reported already for sulfur and nitrogen doped graphene samples.[18,19] These studies showed that adsorption of molecules over graphene with electron donating groups can lead to downshifting and stiffening of the G band.[20]

TGA and DSC data of rGO and S–rGO are shown in Fig. 4. Sublimed sulfur is in the form of $S_8$ rings and converts into a linear polymeric bi-radical molecule (–S–$S_6$–S–) in the temperature range of about ~160 °C by an endothermic reaction called λ-transition.[21] The DSC thermogram of elemental sulfur mainly comprises three endothermic signals: the first one corresponds to the α → β transition of the sulfur at around 100 °C, the second is the melting of β-sulfur which starts at ~120 °C, and the third is the λ-transition which starts at ~160 °C. The sulfur within the S–rGO nanocomposite was completely sublimated at ~330 °C. TGA confirmed the ~49 wt% sulfur loading within the nanocomposite.

The presence of different oxygen functional groups and the bonding of sulfur with oxygen within rGO and S–rGO samples were verified by FTIR (Fig. 5 and S1: ESI†). In the FTIR spectrum of S–rGO, the strong bands at ~3670 cm$^{-1}$ (O–H stretch), 2986–2901 cm$^{-1}$ (C–H stretch), ~1405 cm$^{-1}$ (C–H bends) and 1300–1150 cm$^{-1}$ (C–O stretch of –COOH or S=O stretch of sulfones) suggest the existence of hydroxyl and carboxyl functional groups. The strong peak in the range of 1130–1000 cm$^{-1}$ contains the contributions from the S=O stretch (sulfoxide) and C–O stretch (alcohol group). Moreover, the bands at 950–800 cm$^{-1}$ and ~552 cm$^{-1}$ indicate the bond formation of S–OR (esters) and S–S (disulfide), respectively.

Bright-field TEM (Fig. 6(a)) and SEM (Fig. S2: ESI†) images of the S–rGO illustrate the wrinkled thin layered morphology of the sample.[22] Energy filtered transmission electron microscopy (EFTEM) elemental mappings of the marked area of the TEM image (Fig. 6(a)) using C-K edges and S-L edges are shown in Fig. 6(b) and (c), respectively. From these elemental maps, it is evident that there is uniform distribution of sulfur over the graphene layers. The same can also be observed from the scanning transmission electron microscopy (STEM) image (Fig. 6(d)), where no variations in *z*-contrast are observed.

Open Access Article. Published on 28 October 2015. Downloaded on 6/14/2026 5:48:44 AM.
This article is licensed under a Creative Commons Attribution 3.0 Unported Licence.

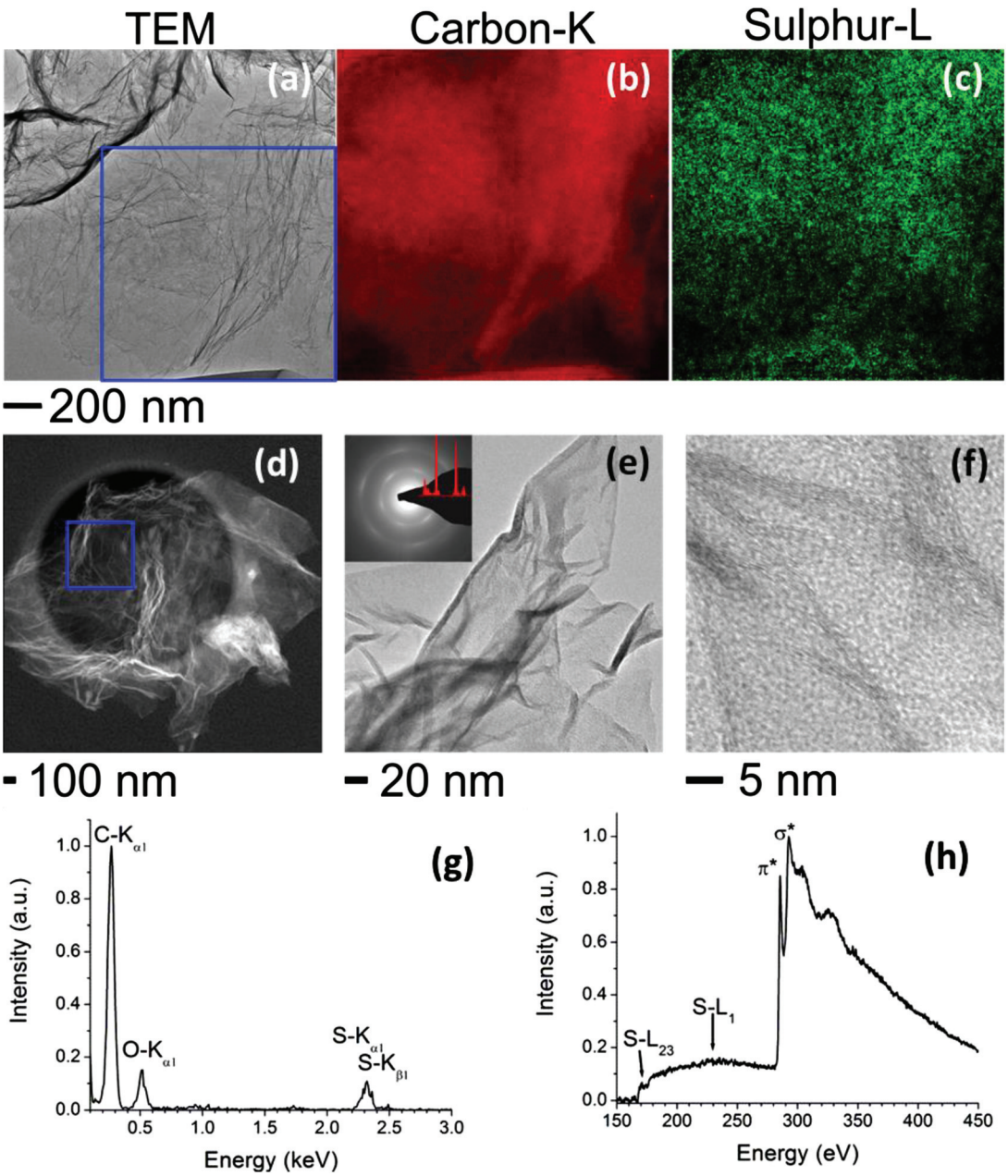


**Fig. 6** (a) Bright-field TEM and EFTEM elemental mapping using (b) C-K edge and (c) S-L edges images of the S–rGO. (d) STEM-HAADF image of S–rGO. (e) Bright-field TEM image of S–rGO accompanied by the corresponding indexed SAED pattern, where the measured *d*-values are 3.54 Å, 2.03 Å, and 1.97 Å from the center of the SAED pattern. (f) High resolution TEM micrograph of S–rGO. (g) Energy dispersive X-ray spectrum and (h) electron energy loss spectrum of S–rGO, corresponding to the area marked in the STEM image.

Fig. 6(e) shows a bright-field TEM image of S–rGO accompanied by the corresponding selected area diffraction (SAED) pattern. The strong texturing observed from the SAED pattern is from the wrinkled morphology of the sample. The *d*-value of the (002) graphitic plane measured from the SAED pattern is ~3.54 Å, which is comparable to the XRD results for S–rGO (*cf.* Fig. 2). The high resolution TEM micrograph (Fig. 6(f)) of S–rGO shows the stacked graphene layer morphology of the sample. The presence of carbon, oxygen and sulfur within the S–rGO nanocomposite was further confirmed by energy dispersive X-ray spectroscopy (Fig. 6(g)) and electron energy loss spectroscopy (Fig. 6(h)), corresponding to the area marked in the STEM image of Fig. 6(d).

To investigate the chemical bonding between different elements such as carbon, oxygen and sulfur in more detail, X-ray photoelectron spectroscopy (XPS) measurements were carried out for rGO and S–rGO samples. The high resolution O 1s spectrum of rGO (Fig. 7(a)) shows two peaks, which can be

 This journal is © The Royal Society of Chemistry 2016

Open Access Article. Published on 28 October 2015. Downloaded on 6/14/2026 5:48:44 AM.
This article is licensed under a Creative Commons Attribution 3.0 Unported Licence.

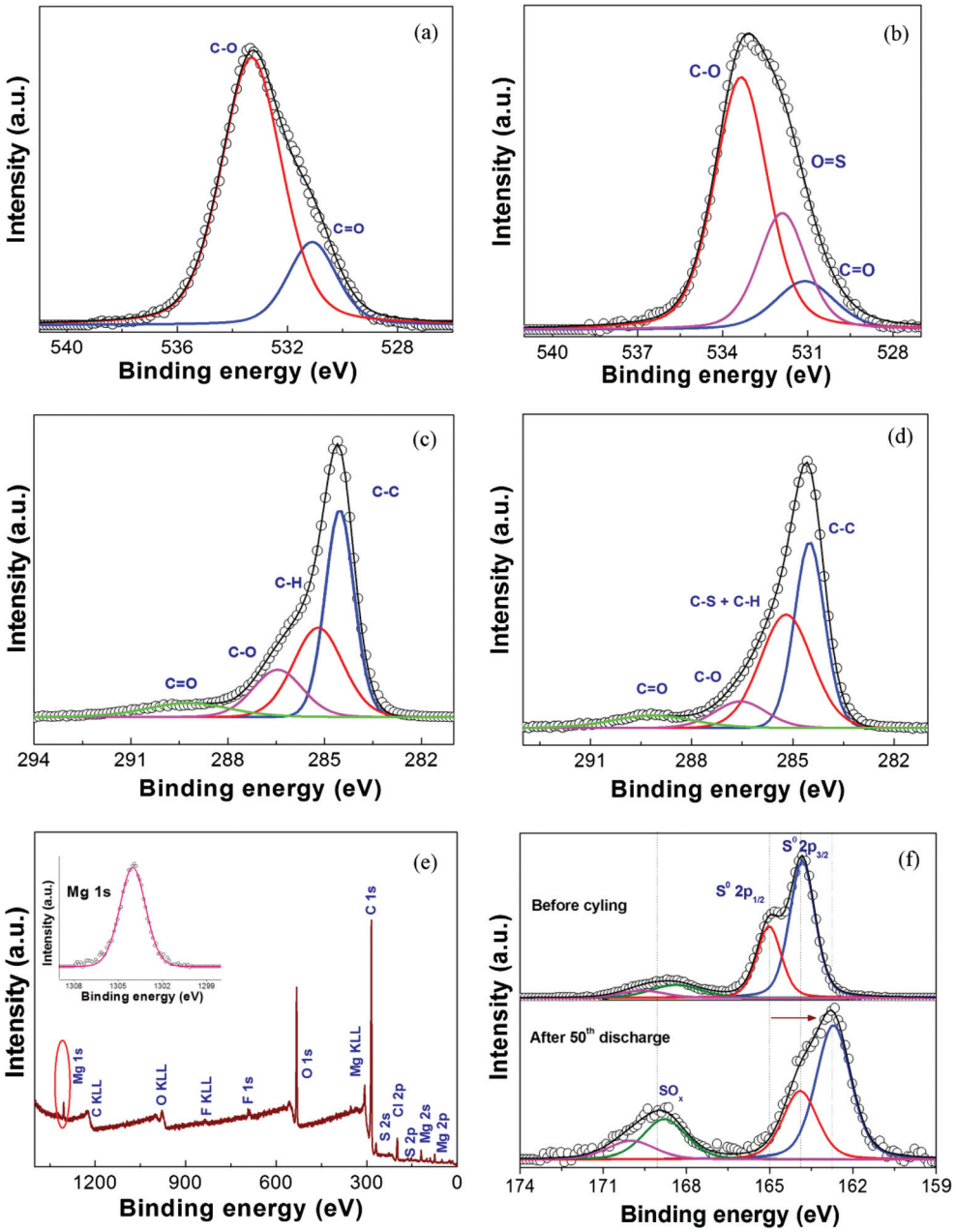


**Fig. 7** (a, b) High resolution O 1s XPS spectra of rGO and S–rGO. (c, d) High resolution C 1s XPS spectra of rGO and S–rGO. (e) XPS survey spectrum of the S–rGO cathode after 50 battery cycles in the discharge state. The inset shows the high resolution Mg 1s XPS spectrum. (f) Comparison of high resolution S 2p XPS spectra of the S–rGO cathode electrode before battery cycling and after 50 cycles in the discharge state.

attributed to C–O (533.1 eV) and C═O (531.3 eV) species, respectively.[23] After sulfur addition (S–rGO, Fig. 7(b)), another peak appears at 531.6 eV, which can be attributed to the formation of S═O bonds.[23] These bond formations let the sulfur immobilize on the rGO surfaces during battery charge/discharge. For example, recent studies of a Li/S battery have shown that oxygen functional groups on a carbon support can bond with polysulfides and thus mitigate the diffusion to the anode side.[24,25] The high-resolution C 1s spectrum of rGO (Fig. 7(c)) also shows the presence of C–O (epoxide *etc.*, at 286.5 eV) and C═O (289.2 eV) bond formation on the graphene substrate; the peaks at 284.5 eV and 285.2 eV are assigned to graphene and C–H (and/or $sp^3$-hybridized C–C) groups, respectively. For the S–rGO sample, an increase of the intensity of the component at 285.2 eV and a decrease of the two peaks at higher binding energy (which we attribute to the bonding of oxygen with carbon) are observed. The binding energy (BE) of carbon with a C–S bond is very close to that with a C–H (or $sp^3$-hybridized C–C) bond,[26,27] and the increase of the peak at 285.2 eV in the spectrum of the S–rGO is there-

Open Access Article. Published on 28 October 2015. Downloaded on 6/14/2026 5:48:44 AM.
This article is licensed under a Creative Commons Attribution 3.0 Unported Licence.

fore assigned to sulfur deposition. A direct proof for the deposition of sulfur over graphene layers and the formation of oxygen–sulfur bond is the S 2p spectrum, which is shown in Fig. 7(f) (see also the discussion below). The reduction of the peaks related to oxygen bound to C after sulfur impregnation is also reflected in the relative oxygen concentrations within the sample surfaces of S–rGO (~10.4 atomic%) and rGO (~12 atomic%), which were derived from the quantitative analysis of the detail spectra. Recent reports have shown that C–S bond formation during sulfur impregnation over GO can reduce the oxygen content within GO.[28]

The electrochemical studies of the Mg/S rechargeable battery system were carried out by building Swagelok type cells with S–rGO as the cathode material and the Mg–carbon composite (80 : 20% w/w, prepared by ball milling) as the anode material. The sulfur loading within the cathode electrode was 1.5 mg $cm^{-2}$. 80 μL of non-nucleophilic electrolyte was used for each cell. The electrolyte was prepared by mixing a non-nucleophilic base of magnesium-bis(hexamethyldisilazide) $[(HMDS)_2Mg]$ with the Lewis acid, $AlCl_3$ (1 : 2 molar ratio), and dissolving the reaction product in a tetraglyme ($C_{10}H_{22}O_5$) ethereal solvent according to chemical reaction (1).[7]

$$2\left[(HMDS)_2Mg\right] + 4AlCl_3 \Leftrightarrow [Mg_2Cl_3][(HMDS)AlCl_3] + 3[(HMDS)AlCl_2] \quad (1)$$

$$[(HMDS)AlCl_2] + 2MgCl_2 \Leftrightarrow [Mg_2Cl_3][(HMDS)AlCl_3] \quad (2)$$

$[Mg_2Cl_3]^+[(HMDS)AlCl_3]^-$ is the electrochemically active complex, while $[(HMDS)AlCl_2]$ is a neutral by-product. To convert the neutral $[(HMDS)AlCl_2]$ by-product into the electrochemically active complex $[Mg_2Cl_3]^+[(HMDS)AlCl_3]^-$ according to reaction (2), $MgCl_2$ was slowly added to the solution obtained by chemical reaction (1). Thus, the Mg ion concentration could be increased up to 1.8 M. Recent studies in a Li/S battery show that polysulfide dissolution to the anode side can be suppressed by increasing the viscosity of the electrolyte solution and enhancing the lithium ion concentration within the electrolyte.[7,29] Inconel 625 was used as the current collectors, which show good corrosion resistance against the chloride containing electrolyte.[30] Cyclic voltammetry (CV) measurements were carried out (Fig. S3: ESI†) to determine the electrochemical window of the electrolyte using a two-electrode cell containing an Inconel disc as the working electrode and Mg as the reference and counter electrodes. The CV shows a reversible Mg deposition capability and a voltage stability of the electrolyte up to 3.2 V.

Fig. 8(a) depicts the first cycle galvanostatic discharge/charge curve of a Mg/S rechargeable battery with S–rGO as the cathode and the Mg–carbon composite as anode electrodes, at a current density of 20 mA $g^{-1}$ and the voltage in the range of 0.5–2.5 V. The capacity values were calculated based on the mass of sulfur at the cathode electrode. The open circuit voltage (OCV) for the fresh cell was stabilized at 1.72 V after 12 hours resting time. The S–rGO nanocomposite delivered a high initial discharge capacity of 1024 mA h $g^{-1}$ and a charge capacity of 548 mA h $g^{-1}$. During the second cycle, the cell gave discharge and charge capacity values of 448 mA h $g^{-1}$ and 396 mA h $g^{-1}$, respectively. The first discharge voltage profile of the Mg/S cell showed two voltage plateaus similar to the Li/S cell.[31,32] The first small plateau in the voltage profile was between 1.72 and 1.3 V and the second plateau was within the range of 1.3–0.7 V. During the discharge, the sulfur within the S–rGO cathode electrode passes through several distinct reductive steps: in the first step, there is a reduction of the solid cyclo-$S_8$ to $S_8^{2-}$ *via* the formation of liquid polysulfide (PS) $MgS_8$, which is subsequently reduced to the PS, $MgS_6$ and then to $MgS_4$.[7,33] Since these polysulfides may be soluble within the electrolyte, the reaction kinetics is fast, which gives the first small voltage plateau with a capacity contribution of ~186 mA h $g^{-1}$ in the discharge curve. In the following reductive steps, liquid $MgS_4$ polysulfide is reduced to solid $MgS_2$ and that gives a second voltage plateau with a capacity contribution of ~700 mA h $g^{-1}$ in the discharge curve. In the final step, $MgS_2$ is reduced to MgS, which represents the tail in the discharge voltage profile. Since the electrochemical reactions at the second plateau and tail of the voltage profiles are more sluggish, the reaction is slowed down and it is difficult to obtain the theoretical capacity (~1675 mA h $g^{-1}$) of the MgS cell.[1,7]

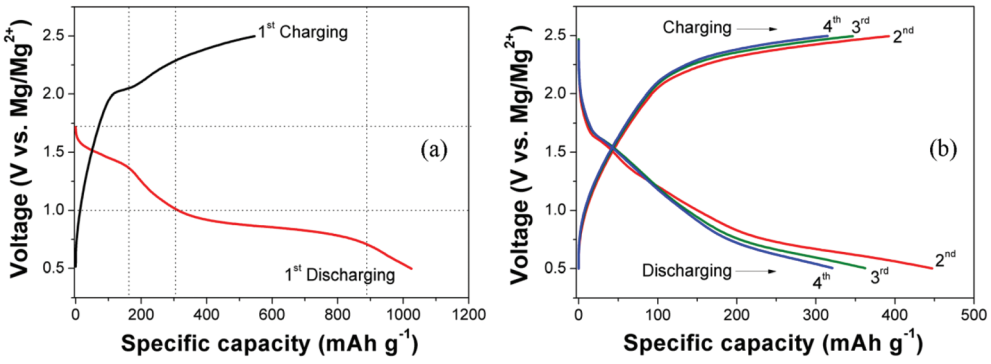


Fig. 8 (a) Initial and (b) 2nd, 3rd and 4th charge–discharge curves of the S–rGO nanocomposite at a current density of 20 mA $g^{-1}$ in the voltage range of 0.5–2.5 V *vs.* $Mg/Mg^{2+}$.

 This journal is © The Royal Society of Chemistry 2016

Open Access Article. Published on 28 October 2015. Downloaded on 6/14/2026 5:48:44 AM.
This article is licensed under a Creative Commons Attribution 3.0 Unported Licence.

Table 1 The discharge/charge capacities of the S–rGO electrode for the initial and final cycles

| Cycle number | Discharge capacity (mA h $g^{-1}$) | Charge capacity (mA h $g^{-1}$) |
|---|---|---|
| 1 | 1024 | 548 |
| 2 | 448 | 396 |
| 3 | 364 | 349 |
| 4 | 323 | 315 |
| 5 | 296 | 294 |
| 6 | 280 | 279 |
| 7 | 266 | 270 |
| 10 | 244 | 260 |
| 15 | 228 | 243 |
| 50 | 219 | 236 |

The overall electrochemical reactions within the Mg/S battery can be represented by the following eqn (3)–(5).[7,33]

$$S_8 + 4e^- + 2Mg^{2+} \rightarrow 2MgS_4 \quad (3)$$

$$MgS_4 + 2e^- + Mg^{2+} \rightarrow 2MgS_2 \quad (4)$$

$$MgS_2 + 2e^- + Mg^{2+} \rightarrow 2MgS \quad (5)$$

The discharge/charge curves for the 2nd, 3rd and 4th cycles are illustrated in Fig. 8(b). The discharge/charge capacities for the initial and final cycles are given in Table 1 and show a major decrease in the capacity from the first to second discharge. From the second discharge onwards, a drop off in the capacity contribution from the first voltage plateau and a merging of the first and second voltage plateau were noticed in the discharge curve. This could be due to $MgS/MgS_2$, which are formed after the first discharge and seem to not convert back completely into elemental sulfur in the later cycles. Thus, a certain amount of high-order Mg polysulfides could remain at the end of charging, similar to Li/S batteries.[10] Hence, after the first cycle, the cathode and the electrolyte may contain different higher order polysulfides from $MgS_8$ to $MgS_4$. The cyclic stability data (Fig. 9(a)) show a capacity fading for the initial cycles similar to what was observed in the Li/S battery system, mainly due to the presence of some sulfur within the cathode, which is going through an irreversible transformation–dissolution process.[34–36] Afterwards, relatively stable cyclic stability was observed for further 50 cycles (see Table 1 and Fig. 9(a)). At the end of the 6th cycle, the discharge and charge capacity values were 280 mA h $g^{-1}$ and 279 mA h $g^{-1}$, respectively. From the 7th cycle onwards, the charge capacity contribution gradually increased as compared to the corresponding discharge capacity. The increase of charge capacity over the discharge capacity after some initial cycles is probably due to the Mg polysulfide shuttle effect, which acts as a parasitic side reaction. At the end of the 50th cycle, the discharge and charge capacity values were 219 mA h $g^{-1}$ and 236 mA h $g^{-1}$, respectively. The current rate capability of the S–rGO cathode material in the Mg/S battery was investigated after running the cell for the initial 10 cycles at the current density of 20 mA $g^{-1}$ and the corresponding discharge/charge voltage profiles are given in Fig. 9(b). The discharge capacities for different current rates are summarized in Table 2. The voltage profiles show that both discharge voltage plateaus and the capacity decrease gradually with increasing current rate, which may be attributed to higher ohmic and kinetic overvoltages at higher current rates and the sluggish kinetics of Mg with S.[8,37]

In comparison with previous results on Mg/S batteries, the present results show progress. Muldoon *et al.* tested a Mg/S battery for the initial two cycles with the first and second discharge capacities of 1200 mA h $g^{-1}$ and 394 mA h $g^{-1}$, respect-

Table 2 The discharge capacities of the S–rGO electrode at different current densities

| Discharge current density (mA $g^{-1}$) | Discharge capacity (mA h $g^{-1}$) |
|---|---|
| 5 | 885 |
| 10 | 530 |
| 15 | 285 |
| 25 | 180 |
| 35 | 130 |
| 45 | 108 |

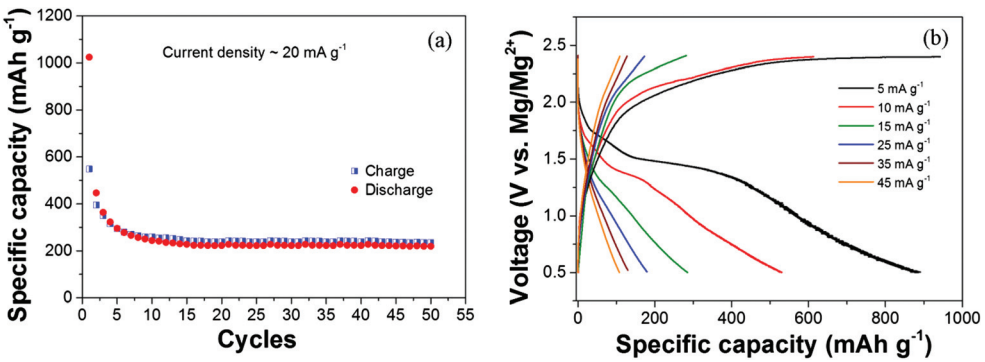


Fig. 9 (a) Cyclic stability of the S–rGO nanocomposite for the initial 50 cycles at the current density of 20 mA $g^{-1}$. (b) Current rate capability of S–rGO electrode for current densities between 5 and 45 mA $g^{-1}$.

Open Access Article. Published on 28 October 2015. Downloaded on 6/14/2026 5:48:44 AM.
This article is licensed under a Creative Commons Attribution 3.0 Unported Licence.

ively, and the voltage plateau was below 0.9 V.[1] The authors observed a clearly visible yellow discolouration of the separator as a result of polysulfide dissolution that contributes to the capacity fading. During the first discharge of this cell, the voltage plateau increased from 0.55 V to 0.89 V due to the breaking of a resistive surface layer on the metallic magnesium anode electrode. In a recent study, Zhao-Karger *et al.* could improve the performance of a Mg/S cell using sulfur loaded poly(ethylene glycol) functionalized mesoporous carbon material (CMK-3) as the cathode electrode along with a non-nucleophilic electrolyte in glyme/ionic liquid solutions.[7] Using the same combination of electrolyte and binder as in our present study, the first discharge capacity of this Mg/S cell was 500 mA h $g^{-1}$ (current density of 20 mA $g^{-1}$) with an initial voltage plateau of about 1.65 V. The authors could run the cell for the initial 20 cycles with a final discharge capacity of 260 mA h $g^{-1}$. In another report, Ha *et al.* presented a Mg/S cell with a first discharge capacity of 500 mA h $g^{-1}$ and a voltage plateau of 0.2 V using 0.3 M $Mg(TFSI)_2$ in a glyme/diglyme mixed solvent electrolyte.[38]

To gain more insight into the battery reaction mechanism, XPS measurements were carried out for the S–rGO cathode (Fig. 7(e and f)) and the Mg/C anode (Fig. S4: ESI†) electrodes after battery cycling in the discharged state. For this purpose, the cells were disassembled in an argon filled glove box. The electrodes were separated, rinsed with anhydrous tetraglyme to remove the electrolyte residues and dried in a vacuum. Subsequently, the electrodes were placed in an inert gas filled chamber and transferred into the XPS vacuum chamber. Fig. 7(e) depicts the XP survey spectrum of the S–rGO cathode after the 50$^{th}$ discharge, which shows the peaks corresponding to Mg such as Mg 1s (1304.0 eV), Mg 2s (89.3 eV) and Mg 2p (50.5 eV), mainly coming from the formation of $MgS_x$. The additional peaks corresponding to fluorine and chlorine within the survey spectrum can be attributed to the binder and some residues of the electrolyte. The inset of Fig. 7(e) shows the high resolution Mg 1s XP spectrum. Fig. 7(f) compares S 2p XP spectra of the S–rGO cathode electrode before battery cycling and after the 50$^{th}$ cycle in the discharged state. The S 2p spectrum of the fresh S–rGO cathode electrode can be deconvoluted into two peak couples. The first one, with peaks at 163.8 and 165.0 eV, corresponds to the S $2p_{3/2}$ and S $2p_{1/2}$ doublet of elemental sulfur; the smaller peak couple at 168.4 and 169.6 eV can be ascribed to the bond formation between sulfur and oxygen functional groups present over the rGO surfaces ($SO_x$), as was already seen in the O(1s) detail spectrum and in the FTIR measurements. After the 50$^{th}$ discharge, a shift of the first peak doublet to lower BE is obvious (now 162.7 and 163.9 eV); this shift confirms the formation of $MgS_x$ ($1 < x < 8$), which has also been reported earlier.[1,7,39] The peak couple at higher BE is attributed to higher oxidation states of sulfur again, *i.e.*, the $SO_x$ bond and $MgSO_y$ containing S–O and S=O bonds.[40] The analysis of the XP spectra of the Mg/C anode electrode after the 50$^{th}$ discharge (Fig. S5: ESI†) shows a small but detectable amount (~0.6%) of sulfur in the form of Mg polysulfides ($MgS_x$).

The important role of rGO as a host matrix for sulfur active materials in battery performance was further confirmed by testing the battery performances of a pure sulfur cathode without rGO (Fig. S5: ESI†) using the same cathode sulfur loading (1.5 mg $cm^{-2}$) and amount of electrolyte (80 μL). The cell shows a drastic capacity fading from the first discharge (111 mA h $g^{-1}$) to the 3$^{rd}$ discharge (2 mA h $g^{-1}$) and failure of the battery for further cycles. This shows clearly that a good porous and conductive host matrix is necessary to cycle a sulfur cathode material, also in a Mg/S rechargeable battery. The influence of oxygen functional groups over rGO on electrochemical battery performance was evaluated by comparing them to rGO material from which part of the oxygen functional groups were removed. For this purpose, the as-prepared rGO was further heat treated to high temperature (900 °C) under vacuum. The FTIR spectrum of this material (Fig. S1: ESI†) shows that the majority of oxygen functional groups were removed from the rGO sample after this treatment. Using this material, the sulfur–rGO (900 °C) composite was prepared by mechanical mixing and the Mg/S cell performance of it was tested under the same experimental conditions (1.5 $mg_{sulfur}$ $cm^{-2}$, 80 μL electrolyte). The first and second discharge capacities for the cell were 479 and 249 mA h $g^{-1}$ (Fig. S6: ESI†), respectively, with a low voltage plateau (~0.7 V). After 15 cycles, the discharge capacity had dropped to 71 mA h $g^{-1}$, while it was 228 mA h $g^{-1}$ for the S–rGO cathode composite (*cf.* Table 1). This performance degradation of S–rGO (900 °C) as compared to the S–rGO cathode indicates the importance of (1) a highly porous morphology of the structure, and (2) the presence of oxygen functional groups over the support for strong adsorption of sulfur and for further formation of Mg polysulfides on the graphene layers during battery cycling.

The Mg/S cell with sulfur dispersed rGO as the cathode electrode gives good cyclability and a better current rate capability due to the special functional and morphological properties of reduced graphene oxide.[1,41] The corresponding electrochemical mechanism is given in the schematic Fig. 10. The two-

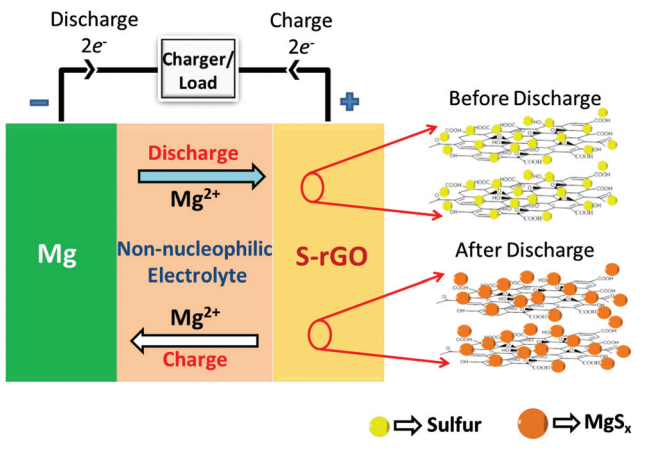


**Fig. 10** (a) Electrochemical mechanism of the S–rGO nanocomposite electrode within a Mg/S cell.


This journal is © The Royal Society of Chemistry 2016

Open Access Article. Published on 28 October 2015. Downloaded on 6/14/2026 5:48:44 AM.
This article is licensed under a Creative Commons Attribution 3.0 Unported Licence.

dimensional, large-surface-area and porous morphology of rGO give more adsorption sites for the dispersion of sulfur and acts as a buffer layer to accommodate the volume changes during the electrochemical conversion reactions between sulfur and Mg upon discharging/charging.[42,43] In addition, the oxygen functional groups present over the surface of rGO, especially carbonyl, epoxy and hydroxyl groups, can bond with sulfur particles and immobilize them and the later formed Mg polysulfides.[25,44] The uniform dispersion of the sulfur particles over the surface of conductive rGO gives an intimate electronic contact between current collector and insulating sulfur active material. Even though the present results on the Mg/S cell using sulfur loaded rGO as the cathode along with a non-nucleophilic electrolyte are promising, further improvements in the reversible capacity and cyclic stability are required. For these, it is necessary to obtain a deeper insight into the Mg polysulfide dissolution and bond formation of Mg polysulfides with different oxygen functional groups.

## 4. Conclusions

We have developed an Mg/S battery with good cyclability using a graphene based sulfur composite electrode and a non-nucleophilic electrolyte. The cell gives a reversible discharge capacity of 448 mA h $g^{-1}$ and a discharge capacity of 236 mA h $g^{-1}$ at the end of the 50$^{th}$ cycle and also a better current rate capability. The oxygen functional groups over the surface of rGO improve bond formation with sulfur particles and help in uniform dispersion. Along with this, rGO acts as a buffer layer, to accommodate the volume changes upon electrochemical cycling between sulfur and MgS, and provides good electronic conductivity and a high surface area for the dispersion of the active material.

## Acknowledgements

Financial support from EU-RTD "Hi-C" ("Novel *in situ* and *in operando* techniques for characterization of interfaces in electrochemical storage systems") in the 7th FP, grant agreement no. 608575, is gratefully acknowledged. B. P. Vinayan acknowledges the Alexander von Humboldt Foundation for research funding. The authors acknowledge the support from the Karlsruhe Nano Micro Facility (KNMF) for electron microscopy and spectroscopy. C.V. acknowledges Prof. Dr Horst Hahn for his continuous support.

## Notes and references

1 H. S. Kim, T. S. Arthur, G. D. Allred, J. Zajicek, J. G. Newman, A. E. Rodnyansky, A. G. Oliver, W. C. Boggess and J. Muldoon, *Nat. Commun.*, 2011, **2**, 427.
2 T. D. Gregory, R. J. Hoffman and R. C. Winterton, *J. Electrochem. Soc.*, 1990, **137**, 775–780.
3 M. Jäckle and A. Groß, *J. Chem. Phys.*, 2014, **141**, 174710.
4 X. Ji, K. T. Lee and L. F. Nazar, *Nat. Mater.*, 2009, **8**, 500–506.
5 O. Tutusaus and R. Mohtadi, *ChemElectroChem*, 2015, **2**, 51–57.
6 Z. Zhao-Karger, X. Zhao, O. Fuhr and M. Fichtner, *RSC Adv.*, 2013, **3**, 16330–16335.
7 Z. Zhao-Karger, X. Zhao, D. Wang, T. Diemant, R. J. Behm and M. Fichtner, *Adv. Energy Mater.*, 2014, **5**, 1401155.
8 P. Saha, M. K. Datta, O. I. Velikokhatnyi, A. Manivannan, D. Alman and P. N. Kumta, *Prog. Mater. Sci.*, 2014, **66**, 1–86.
9 A. Manthiram, Y. Fu and Y.-S. Su, *Acc. Chem. Res.*, 2012, **46**, 1125–1134.
10 D. Moy, A. Manivannan and S. R. Narayanan, *J. Electrochem. Soc.*, 2015, **162**, A1–A7.
11 Y. V. Mikhaylik and J. R. Akridge, *J. Electrochem. Soc.*, 2004, **151**, A1969–A1976.
12 Y. Sun, Q. Wu and G. Shi, *Energy Environ. Sci.*, 2011, **4**, 1113–1132.
13 J. Hou, Y. Shao, M. W. Ellis, R. B. Moore and B. Yi, *Phys. Chem. Chem. Phys.*, 2011, **13**, 15384–15402.
14 B. P. Vinayan, N. I. Schwarzburger and M. Fichtner, *J. Mater. Chem. A*, 2015, **3**, 6810–6818.
15 W. S. Hummers and R. E. Offeman, *J. Am. Chem. Soc.*, 1958, **80**, 1339–1339.
16 B. P. Vinayan, R. Nagar and S. Ramaprabhu, *J. Mater. Chem.*, 2012, **22**, 25325–25334.
17 M. S. Dresselhaus, G. Dresselhaus and M. Hofmann, *Philos. Trans. R. Soc., A*, 2008, **366**, 231–236.
18 J.-E. Park, Y. J. Jang, Y. J. Kim, M.-S. Song, S. Yoon, D. H. Kim and S.-J. Kim, *Phys. Chem. Chem. Phys.*, 2014, **16**, 103–109.
19 Z.-H. Sheng, L. Shao, J.-J. Chen, W.-J. Bao, F.-B. Wang and X.-H. Xia, *ACS Nano*, 2011, **5**, 4350–4358.
20 H. Liu, Y. Liu and D. Zhu, *J. Mater. Chem.*, 2011, **21**, 3335–3345.
21 G. Carotenuto, V. Romeo, S. De Nicola and L. Nicolais, *Nanoscale Res. Lett.*, 2013, **8**, 94.
22 S. U. Yu, B. Park, Y. Cho, S. Hyun, J. K. Kim and K. S. Kim, *ACS Nano*, 2014, **8**, 8662–8668.
23 F. Wu, J. Li, Y. Tian, Y. Su, J. Wang, W. Yang, N. Li, S. Chen and L. Bao, *Sci. Rep.*, 2015, **5**, 13340.
24 J. Song, T. Xu, M. L. Gordin, P. Zhu, D. Lv, Y.-B. Jiang, Y. Chen, Y. Duan and D. Wang, *Adv. Funct. Mater.*, 2014, **24**, 1243–1250.
25 L. Ji, M. Rao, H. Zheng, L. Zhang, Y. Li, W. Duan, J. Guo, E. J. Cairns and Y. Zhang, *J. Am. Chem. Soc.*, 2011, **133**, 18522–18525.
26 G. Hui, L. Zheng, S. Li, G. Wenhua, G. Wei, C. Lijie, R. Amrita, Q. Weijin, V. Robert and M. A. Pulickel, *Nanotechnology*, 2012, **23**, 275605.
27 H. R. Thomas, A. J. Marsden, M. Walker, N. R. Wilson and J. P. Rourke, *Angew. Chem., Int. Ed.*, 2014, **53**, 7613–7618.
28 W. Chen, L. Yan and P. R. Bangal, *J. Phys. Chem. C*, 2010, **114**, 19885–19890.
29 E. S. Shin, K. Kim, S. H. Oh and W. I. Cho, *Chem. Commun.*, 2013, **49**, 2004–2006.

Open Access Article. Published on 28 October 2015. Downloaded on 6/14/2026 5:48:44 AM.
This article is licensed under a Creative Commons Attribution 3.0 Unported Licence.

30 C. Wall, Z. Zhao-Karger and M. Fichtner, *ECS Electrochem. Lett.*, 2015, **4**, C8–C10.
31 Z. Wang, Y. Dong, H. Li, Z. Zhao, H. Bin Wu, C. Hao, S. Liu, J. Qiu and X. W. Lou, *Nat. Commun.*, 2014, **5**, 5002.
32 S. Lu, Y. Chen, X. Wu, Z. Wang and Y. Li, *Sci. Rep.*, 2014, **4**, 4629.
33 D.-W. Wang, Q. Zeng, G. Zhou, L. Yin, F. Li, H.-M. Cheng, I. R. Gentle and G. Q. M. Lu, *J. Mater. Chem. A*, 2013, **1**, 9382–9394.
34 G. He, X. Ji and L. Nazar, *Energy Environ. Sci.*, 2011, **4**, 2878–2883.
35 S. Thieme, J. Bruckner, A. Meier, I. Bauer, K. Gruber, J. Kaspar, A. Helmer, H. Althues, M. Schmuck and S. Kaskel, *J. Mater. Chem. A*, 2015, **3**, 3808–3820.
36 J. Schuster, G. He, B. Mandlmeier, T. Yim, K. T. Lee, T. Bein and L. F. Nazar, *Angew. Chem., Int. Ed.*, 2012, **51**, 3591–3595.
37 M. Winter and R. J. Brodd, *Chem. Rev.*, 2004, **104**, 4245–4270.
38 S.-Y. Ha, Y.-W. Lee, S. W. Woo, B. Koo, J.-S. Kim, J. Cho, K. T. Lee and N.-S. Choi, *ACS Appl. Mater. Interfaces*, 2014, **6**, 4063–4073.
39 R. S. C. Smart, W. M. Skinner and A. R. Gerson, *Surf. Interface Anal.*, 1999, **28**, 101–105.
40 Y. Diao, K. Xie, S. Xiong and X. Hong, *J. Electrochem. Soc.*, 2012, **159**, A1816–A1821.
41 M. Xiao, M. Huang, S. Zeng, D. Han, S. Wang, L. Sun and Y. Meng, *RSC Adv.*, 2013, **3**, 4914–4916.
42 B. P. Vinayan and S. Ramaprabhu, *J. Mater. Chem. A*, 2013, **1**, 3865–3871.
43 J. Jin, Z. Wen, G. Ma, Y. Lu, Y. Cui, M. Wu, X. Liang and X. Wu, *RSC Adv.*, 2013, **3**, 2558–2560.
44 J. W. Kim, J. D. Ocon, D.-W. Park and J. Lee, *J. Energy Chem.*, 2013, **22**, 336–340.


This journal is © The Royal Society of Chemistry 2016